# scientific reports

OPEN

# Advances in physicochemical characterization of lead-free hybrid perovskite [NH$_3$(CH$_2$)$_3$NH$_3$]CuBr$_4$ crystals

Ae Ran Lim[1,2]✉ & Lee Ku Kwac[1,3]

To support the development of eco-friendly hybrid perovskite solar cells, structural, thermal, and physical properties of the lead-free hybrid perovskite [NH$_3$(CH$_2$)$_3$NH$_3$]CuBr$_4$ were investigated using X-ray diffraction (XRD), differential scanning calorimetry, thermogravimetric analysis, and nuclear magnetic resonance spectroscopy. The crystal structure confirmed by XRD was monoclinic, and thermodynamic stability was observed at approximately 500 K without any phase transition. The large changes in the $^1$H chemical shifts of NH$_3$ and those in C2 close to N are affected by N–H⋯Br hydrogen bonds because the structural geometry of CuBr$_4$ changed significantly. The $^1$H and $^{13}$C spin–lattice relaxation times (T$_{1\rho}$) showed very similar molecular motions according to the Bloembergen–Purcell–Pound theory at low temperatures; however, the $^1$H T$_{1\rho}$ values representing energy transfer were about 10 times lesser than those of $^{13}$C T$_{1\rho}$. Finally, the $^1$H and $^{13}$C T$_{1\rho}$ values of [NH$_3$(CH$_2$)$_3$NH$_3$]$Me$Br$_4$ ($Me$ = Cu, Zn, and Cd) were compared with those reported previously. $^1$H T$_{1\rho}$ was affected by the paramagnetic ion of the anion, while $^{13}$C T$_{1\rho}$ was affected by the $Me$Br$_4$ structure of the anion; $^{13}$C T$_{1\rho}$ values in $Me$ = Cu and Cd with the octahedral $Me$Br$_6$ structure had longer values than those in $Me$ = Zn with the tetrahedral $Me$Br$_4$ structure. We believe that these detailed insights on the physical properties will play a crucial role in the development of eco-friendly hybrid perovskite solar cells.

The development of solar cells based on CH$_3$NH$_3$Pb$X_3$ ($X$ = Cl, Br, and I) type organic–inorganic hybrid materials have advanced recently. However, due to the presence of Pb, these perovskites decompose in humid air and are toxic. Therefore, the development of alternative eco-friendly hybrid perovskite solar cells is crucial[1–5]. The synthesis of novel groups of organic–inorganic materials, as well as improved functional materials, has attracted significant attention. The fabrication of hybrid perovskites has recently been reported as a major challenge in the context of developing ferroelastic semiconductors[6]. On the other hand, the success of single-crystal-level ferroelectric performance makes hybrid perovskites suitable candidates for flexible and wearable devices[7,8]. As an eco-friendly alternative to sunlight, the need for detailed characterization of perovskite structures and dynamics of the new organic–inorganic hybrid compounds [NH$_3$(CH$_2$)$_n$NH$_3$]$Me$X$_4$ ($Me$ = Mn, Fe, Co, Cu, and Cd, $n$ = 2, 3 …) with various configurations is increasing in relation to their potential applications in photovoltaic performance[9–18]. Perovskites comprising [NH$_3$(CH$_2$)$_n$NH$_3$] and $Me$X$_4$-layered metal-halogen anionic sublattices are an interesting group of hybrid materials[16,19–25]. Their physicochemical properties are related to their structure and the interaction between the organic and inorganic components. The organic cations are related to the structural flexibility and optical properties, and the inorganic anions are related to the thermal and mechanical properties[26]. For $Me$ = Mn, Cu, or Cd, the structure is two-dimensional and comprises a corner-shared octahedral ($Me$X$_6$)$^{2-}$ with alternating organic layers. When $Me$ = Co or Zn, the structures are tetrahedral ($Me$X$_4$)$^{2-}$ groups sandwiched between layers of organic cations and are zero-dimensional[9,16,20,27]. In [NH$_3$(CH$_2$)$_n$NH$_3$]$Me$X$_4$, the N–H⋯$X$ hydrogen bonding occurs between the NH$_3$ groups at both ends of the organic chains and $X$ group of the perovskite-type layer. Among these materials, [NH$_3$(CH$_2$)$_3$NH$_3$]CuBr$_4$ [bis (propylene-1, 3-diammonium) tetrabromocuprate] with $n$ = 3, $Me$ = Cu, and $X$ = Br has a monoclinic structure with the $P2_1/n$ space group at room temperature. The unit cell dimensions are $a$ = 8.086 Å, $b$ = 7.566 Å, $c$ = 17.622 Å, $\beta$ = 96.75°, and Z = 4[28]. The structural geometry of [NH$_3$(CH$_2$)$_3$NH$_3$]CuBr$_4$ is shown in Fig. 1 (CCDC: 1278590)[28]. The structure is composed of puckered layers of CuBr$_6$ octahedra separated by layers of [NH$_3$(CH$_2$)$_3$NH$_3$]$^{2+}$ chains that are nearly

$^1$Graduate School of Carbon Convergence Engineering, Jeonju University, Jeonju 55069, Korea. $^2$Department of Science Education, Jeonju University, Jeonju 55069, Korea. $^3$Institute of Carbon Technology, Jeonju University, Jeonju 55069, Korea. ✉email: arlim@jj.ac.kr
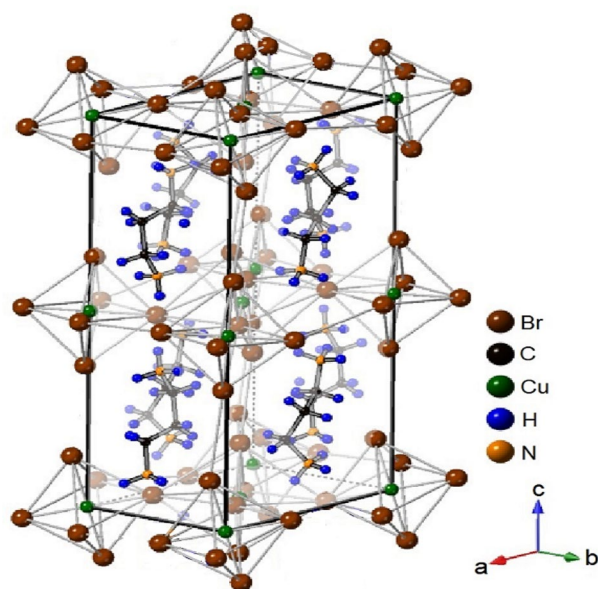
**Figure 1.** Crystal structure of $[NH_3(CH_2)_3NH_3]CuBr_4$ (CCDC: 1278590).

perpendicular to the layers. At both ends of the cation, ammonium groups were located between the layers. Extensive N–H⋯Br type hydrogen bonding was found between the Cu and Br layers and the alkylammonium chain. The organic chains extended along the crystallographic c-direction.

Several reports have been published on related materials. For example, Snively et al.[29] reported the two-halide linear super-exchange bridge of the $[NH_3(CH_2)_3NH_3]CuBr_4$ crystal, and Straatman et al.[30] discussed the theoretical analysis of double-halide super-exchange. Kite and Drumheller[31] conducted an electron paramagnetic resonance study of this crystal in a temperature range below the room temperature. Kallel et al.[32] determined structure of $[NH_3(CH_2)_3NH_3]ZnBr_4$ for *Me*=Zn by X-ray diffraction (XRD) analysis. The $[NH_3(CH_2)_3NH_3]CdBr_4$ crystal structure for *Me*=Cd has been reported by XRD analysis at room temperature, and the temperature dependence of the $^{79,81}$Br nuclear quadrupole resonance spectrum near the phase transition temperatures was studied by Ishihara et al.[33,34] Recently, our group reported the results for $[NH_3(CH_2)_3NH_3]MeBr_4$ (*Me*=Zn and Cd) single crystal studies[27,35]; physicochemical properties and structural dynamics were mainly studied from the chemical shifts and spin-lattice relaxation times using nuclear magnetic resonance (NMR).

The structure and lattice constant of the $[NH_3(CH_2)_3NH_3]CuBr_4$ single crystal grown in this study was confirmed by XRD. To understand the role of inorganic anions on the thermodynamic properties, differential scanning calorimetry (DSC) and thermogravimetric analysis (TGA) experiments were performed. In addition, the role of the organic cation in the structural properties was considered in detail using the magic angle spinning (MAS) NMR method. The chemical shifts and spin-lattice relaxation times $T_{1\rho}$ are discussed for $^1$H and $^{13}$C. In particular, the N–H⋯Br hydrogen bond between the Cu and Br layer and the cation within $[NH_3(CH_2)_3NH_3]CuBr_4$ is expected to provide important characteristics for the development of perovskite material based solar cells. Finally, the physical properties of $[NH_3(CH_2)_3NH_3]MeBr_4$ (*Me*=Cu, Zn, and Cd) crystals were compared with the previous reports and explained based on the paramagnetic ion and the structure of the $MeX_4$ anion.

## Methods

**Materials.** $[NH_3(CH_2)_3NH_3]CuBr_4$ crystals were prepared with molecular weights of $NH_2(CH_2)_3NH_2·2HBr$ and $CuBr_2$ with 1:1 ratio in an aqueous solution. The mixture was stirred and heated to obtain a homogeneous solution. The resulting solution was filtered and brown colored single crystals were obtained by slow evaporation over few weeks. The crystals grew into rectangular shapes with dimensions of $5 \times 5 \times 1$ mm$^3$.

**Characterization.** The structure of the $[NH_3(CH_2)_3NH_3]CuBr_4$ crystal at 298 K was determined by single-crystal XRD system (Bruker D8 Venture, Germany) with Mo-Kα radiation at the Western Seoul Center of the Korea Basic Science Institute (KBSI). DSC (TA Instruments, DSC 25, USA) was performed at a heating rate of 10 °C/min in the 190-600 K temperature range in a $N_2$ gas atmosphere. Thermogravimetric analysis (TGA) was conducted using a thermogravimetric analyzer (TA Instruments, USA) in the 300–680 K temperature range at the same heating rate. Optical observations were performed using a Carl Zeiss microscope equipped with a Linkam THM-600 heating stage.

NMR spectra of the $[NH_3(CH_2)_3NH_3]CuBr_4$ crystals were collected on a Bruker Avance II+ NMR spectrometer at the same KBSI center. The Larmor frequencies for the $^1$H NMR and $^{13}$C NMR experiments were 400.13 and 100.61 MHz, respectively. NMR chemical shifts were referenced to tetramethylsilane (TMS) as the standard. The powdered sample in the cylindrical zirconia rotor was spun at a rate of 10 kHz in the MAS NMR experiment. The spin-locking field during the $^1$H and $^{13}$C NMR acquisition was 71.42 kHz. The $^1$H $T_{1\rho}$ and $^{13}$C $T_{1\rho}$ values were
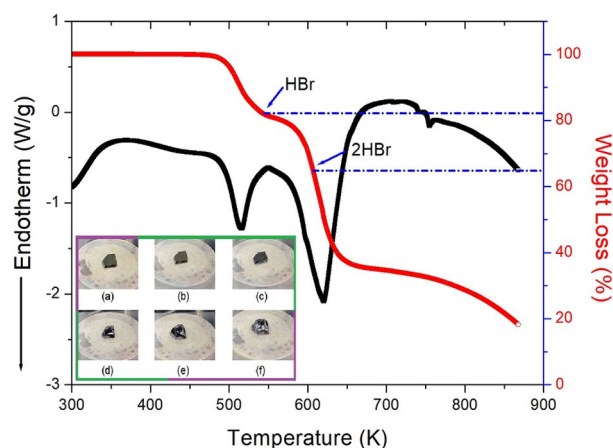
**Figure 2.** Thermogravimetric analysis (TGA) and differential thermal analysis (DTA) curves of [NH$_3$(CH$_2$)$_3$NH$_3$]CuBr$_4$ (inset: Changes in crystal measured by optical polarizing microscopy at (**a**) 300, (**b**) 453, (**c**) 500, (**d**) 543, (**e**) 593, and (**f**) 621 K).

measured by changing the spin-locking pulse duration. $^1$H and $^{13}$C NMR data were measured using a single pulse sequence with a pulse width of 3.25–3.59 μs. NMR data could not be measured at temperatures above 430 K because NMR equipment that could measure at such high temperatures are unavailable.

## Experimental results

**Crystal structure.** Single-crystal XRD analysis of [NH$_3$(CH$_2$)$_3$NH$_3$]CuBr$_4$ was performed at 298 K. The structure, lattice constants, and space group of this crystal were monoclinic, with $a$ = 8.052 ± 0.009 Å, $b$ = 7.560 ± 0.009 Å, $c$ = 17.611 ± 0.190 Å, β = 96.920 ± 0.05°, Z = 4, and $P2_1/n$, and this result was in good agreement with a previous report by Halvorson and Willett[28].

**Thermodynamic property.** In the DSC experiment, there was no phase transition temperature in the 200–500 K range; however, large exothermic peaks were observed at 546 and 577 K (Supplementary Information 1). To confirm that the DSC peaks at 546 and 577 K are related to the phase transition, TGA and differential thermal analysis (DTA) experiments were performed; the results are shown in Fig. 2. The TGA results revealed that this crystal is thermally stable up to 504 K. The initial weight loss of [NH$_3$(CH$_2$)$_3$NH$_3$]CuBr$_4$ began at 504 K, and there was no weight loss before the decomposition temperature. In the TGA curve, [NH$_3$(CH$_2$)$_3$NH$_3$]CuBr$_4$ exhibited a two-stage decomposition at high temperatures. The initial weight loss (17%) occurred in the 500–550 K range, which may be due to the decomposition of HBr in [NH$_3$(CH$_2$)$_3$NH$_3$]CuBr$_4$. The second-stage decomposition (63%) occurred because of the presence of an inorganic moiety in the 550–650 K range. The amount that remained as a solid was calculated from the TGA data and chemical reactions. The weight losses of 17 and 35% at approximately 546 and 607 K are likely due to the decomposition of the HBr and 2HBr moieties, respectively, which is consistent with the exothermic peak in the DSC curve. The molecular weight decreased abruptly between 550 and 650 K, with a corresponding weight loss of 63% at approximately 650 K.

Further, optical polarizing microscopy experiments were conducted to understand the thermal decomposition and melting phenomena of the crystals. The crystal was brown at 300 K, as shown in the inset of Fig. 2. While no changes were observed from 300 to 500 K, the crystal began to melt slightly and changed from brown to dark brown at approximately 543 K. The color change was likely due to decomposition from the loss of HBr, and also due to the geometrical changes in CuBr$_4$. Above 600 K, the surface and edges melted significantly. The thermogram clearly indicated that 543 K was the melting point of the crystal. Hence, the [NH$_3$(CH$_2$)$_3$NH$_3$]CuBr$_4$ crystal is suitable for applications up to 504 K.

**$^1$H NMR chemical shifts and spin–lattice relaxation times.** The $^1$H NMR chemical shifts of the [NH$_3$(CH$_2$)$_3$NH$_3$]CuBr$_4$ crystals were recorded while increasing the temperature, as shown in Fig. 3. Below 270 K, only one $^1$H resonance signal was observed, and the intensity and line-width of the $^1$H signal were very small and wide, respectively, making the detection challenging. The resonance signal exhibited asymmetric shapes owing to the overlapping of the two types of NH$_3$ and CH$_2$ signals. The $^1$H NMR chemical shift for CH$_2$ was recorded at δ = 5.51 ppm at 300 K, whereas that for NH$_3$ was recorded at δ = 10.94 ppm, which subsequently split into two resonance lines. The spinning sidebands for CH$_2$ are represented by open circles and those for NH$_3$ are represented by crosses. The $^1$H chemical shifts for CH$_2$, shown by the dotted line in Fig. 3, did not significantly change with increasing temperature, whereas the change in the $^1$H chemical shifts for NH$_3$ toward the lower chemical shift as the temperature increased. The greater shift in the $^1$H NMR chemical shift of the NH$_3$ in the cation with changes in the temperature, than that of the CH$_2$ is reason for the large change in the N–H···Br hydrogen bonding between the Br around Cu and the H of NH$_3$.

The relationship of the decay rate of proton magnetization is defined by $T_{1\rho}$ and the Eq. (1)[27,36–39]
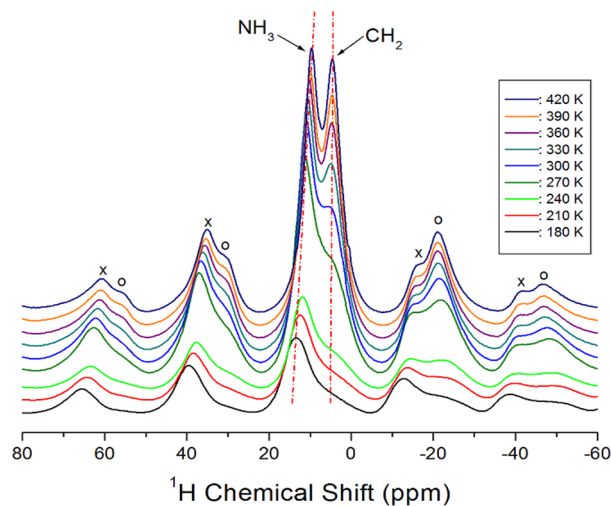
**Figure 3.** $^1H$ NMR chemical shifts for $NH_3$ and $CH_2$ in $[NH_3(CH_2)_3NH_3]CuBr_4$ at several temperatures.
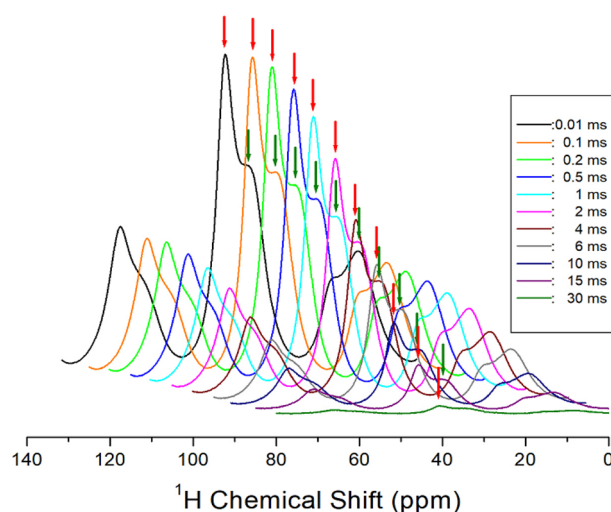


**Figure 4.** Inversion recovery traces for $^1H$ NMR chemical shifts according to the delay time from 0.01 to 30 ms at 300 K.

$$P(\tau) = P(0)\exp(-\tau/T_{1\rho}), \tag{1}$$

where $P(\tau)$ and $P(0)$ are the signal intensities at times $\tau$ and $\tau = 0$, respectively. The intensity changes observed in the $^1H$ NMR spectra were recorded with changing delay times at a given temperature, and at 300 K, the $^1H$ NMR spectrum was plotted with a delay time ranging from 0.01 to 30 ms as shown in Fig. 4. From the slope of the intensities of the $^1H$ signal indicated by the arrow vs. delay times, the $^1H$ $T_{1\rho}$ could be calculated using Eq. (1). As a result, the $^1H$ $T_{1\rho}$ values for $CH_2$ and $NH_3$ are shown in Fig. 5 as a function of the inverse temperature. The $^1H$ $T_{1\rho}$ values were in the order of a few milliseconds for $CH_2$ and $NH_3$, and their values were temperature-dependent. As shown in the cation structure in Fig. 5, the $^1H$ of $CH_2$ is expressed in red, and the $^1H$ of $NH_3$ is expressed in black, which is the same as the $T_{1\rho}$ values. The $T_{1\rho}$ values decreased as the temperature increased and then increased sharply again at 210 K. Below 300 K, only the $^1H$ $T_{1\rho}$ value for $NH_3$ is shown, and the $^1H$ $T_{1\rho}$ values of $CH_2$ above 300 K have longer $T_{1\rho}$ values than $^1H$ of $NH_3$. The $T_{1\rho}$ vs. inverse temperature curve showed a minima of 5.80 ms at 210 K, which indicates the existence of distinct molecular motions. The $T_{1\rho}$ values can be explained by the correlation time $\tau_C$ for the molecular motion. The $T_{1\rho}$ value for the molecular motion based on the Bloembergen–Purcell–Pound (BPP) theory is given by[35–39]:

$$1/T_{1\rho} = G(\gamma_H\gamma_C\hbar/r^3)^2[4F_a + F_b + 3F_c + 6F_d + 6F_e] \tag{2}$$

where $F_a = \tau_C/[1 + \omega_1^2\tau_C^2]$, $F_b = \tau_C/[1 + (\omega_C - \omega_H)^2\tau_C^2]$, $F_c = \tau_C/[1 + \omega_C^2\tau_C^2]$, $F_d = \tau_C/[1 + (\omega_C + \omega_H)^2\tau_C^2]$, and $F_e = \tau_C/[1 + \omega_H^2\tau_C^2]$. Here, G is a coefficient, $\gamma_H$ and $\gamma_C$ are the gyromagnetic ratios of the proton and carbon,
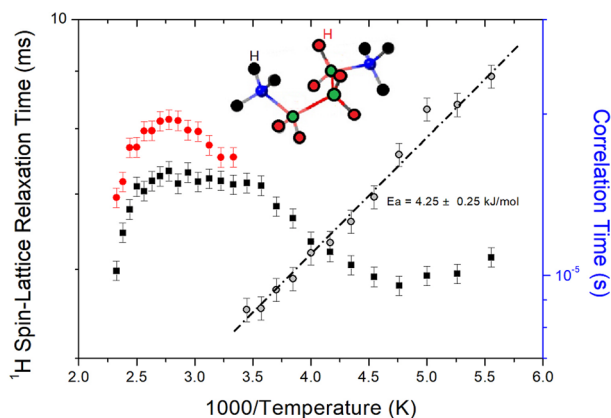
**Figure 5.** $^1H$ NMR spin–lattice relaxation times $T_{1\rho}$ and correlation times for $NH_3$ and $CH_2$ in $[NH_3(CH_2)_3NH_3]CuBr_4$ as a function of inverse temperature.



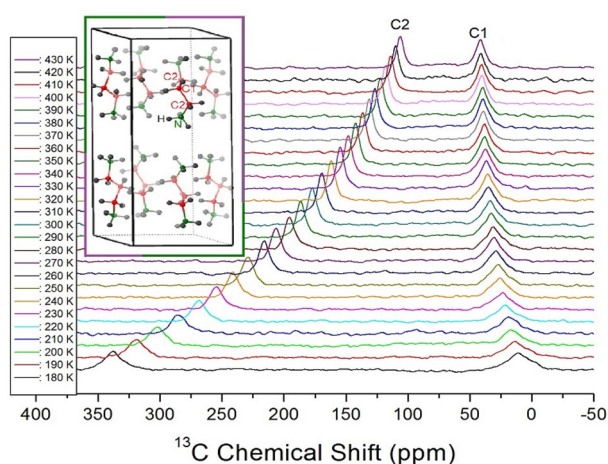**Figure 6.** $^{13}C$ NMR chemical shifts in $[NH_3(CH_2)_3NH_3]CuBr_4$ as a function of temperature (Inset: structure of $[NH_3(CH_2)_3NH_3]$ cation).

respectively, ħ is the reduced Planck constant, $\omega_H$ and $\omega_C$ are the Larmor frequencies of $^1H$ and $^{13}C$, respectively, $r$ is the distance between the proton and carbon, and $\omega_1$ is the spin-locking pulse sequence with a locking pulse of 71.42 kHz. In the rotating frame, $\tau_C$ can be obtained when $\omega_1\tau_C = 1$, and the coefficient G in Eq. (2) can be obtained from $T_{1\rho}$, $\omega_H$, $\omega_C$, and $\omega_1$. Using this G value, $\tau_C$ was obtained as a function of inverse temperature. The local field fluctuation is governed by the thermal motion, which is activated by thermal energy. Therefore, $\tau_C$ is represented by the Arrhenius behavior: $\tau_C = \tau_o\exp(-E_a/k_BT)$, where $E_a$ and $k_B$ are the activation energy and Boltzmann constant, respectively[36]. The $\tau_C$ vs. 1000/T was plotted on a logarithmic scale (inset of Fig. 5), and the $E_a$ of $^1H$, depending on the molecular dynamics, was obtained using 4.25 ± 0.25 kJ/mol by dot line.

### $^{13}C$ NMR chemical shifts and spin–lattice relaxation times.

The $^{13}C$ NMR chemical shifts of $[NH_3(CH_2)_3NH_3]CuBr_4$ were measured as a function of temperature, as shown in Fig. 6. The $^{13}C$ MAS NMR spectra exhibited two resonance signals at all temperatures. The $^{13}C$ NMR spectrum for TMS was recorded at 38.3 ppm at 300 K and was used to determine the exact chemical shift of $^{13}C$[27]. Here, the $CH_2$ between the two $CH_2$ groups is labeled C1, and the $CH_2$ close to $NH_3$ is labeled C2, as shown in the inset of Fig. 6. The two resonance signals at 300 K were recorded at chemical shifts of $\delta = 33.54$ and $\delta = 177.07$ ppm for C1 and C2, respectively. The $^{13}C$ chemical shifts for $CH_2$ were different for C1 far from those of $NH_3$ and C2 close to that of $NH_3$. The $^{13}C$ chemical shift for C1 changed slowly and did not vary significantly with increasing temperature, whereas that for C2 moved abruptly to the lower chemical-shift side with increasing temperature compared to that for C1.

The changes in the intensities of the $^{13}C$ NMR spectral peaks with increasing delay times were measured at a given temperature in the same manner as the $^1H$ $T_{1\rho}$ measurement method. The $^{13}C$ $T_{1\rho}$ values from the slope of the recovery traces are described by a single exponential function in Eq. (1). The $T_{1\rho}$ values for C1 and C2 as a function of 1000/temperature are shown in Fig. 7. In the cation structure, C1 is shown in green, C2 is shown
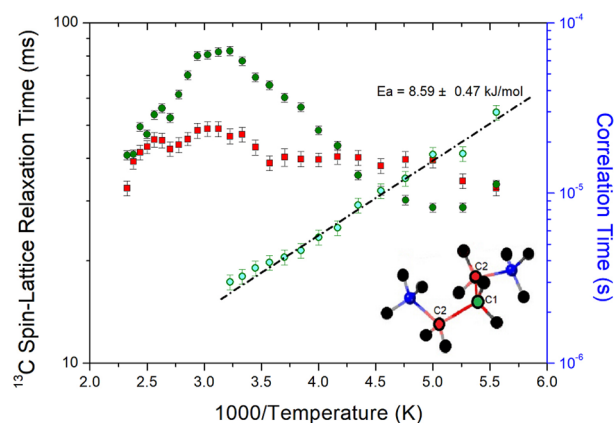
5

**Figure 7.** $^{13}$C NMR spin–lattice relaxation times $T_{1\rho}$ and correlation times for C1 and C2 of $[NH_3(CH_2)_3NH_3]$ $CuBr_4$ as a function of inverse temperature.

| *Me* | Cu | Zn | Cd |
|---|---|---|---|
| Structure | Monoclinic | Monoclinic | Orthorhombic |
| Lattice constants (Å) | a = 8.086 | a = 11.084 | a = 7.898 |
|  | b = 7.566 | b = 10.968 | b = 7.721 |
|  | c = 17.622 | c = 11.185 | c = 19.054 |
|  | β = 96.75 | β = 117.07 |  |
| $T_C$ (K) | x | 272 | 326, 368 |
| $^1$H $T_{1\rho}$ (ms) at 300 K | 7.14 (for NH$_3$) | 236.38 | 280.16 |
|  | 7.55 (for CH$_2$) |  |  |
| $^{13}$C $T_{1\rho}$ (ms) at 300 K | 77.19 (for C1) | 6.80 (for C1) | 81.59 (for C1) |
|  | 47.00 (for C2) | 5.86 (for C2) | 59.79 (for C2) |

**Table 1.** Structure, lattice constants, phase transition temperature $T_C$, and spin–lattice relaxation time $T_{1\rho}$ of $[NH_3(CH_2)_3NH_3]Me Br_4$ (*Me* = Cu, Zn, and Cd) crystals.

in red, and $T_{1\rho}$ is shown in the same way. $^{13}$C $T_{1\rho}$ values for C2 showed no changes in the temperature range measured in this study, and the $T_{1\rho}$ for C1 according to the temperature change showed a similar trend as that for $^1$H $T_{1\rho}$. The $^{13}$C $T_{1\rho}$ values were approximately 10 times longer than the $^1$H $T_{1\rho}$ values. The $^{13}$C $T_{1\rho}$ values were unaffected by the spin diffusion owing to the small dipolar coupling, which results from the low natural abundance. On the other hand, the $T_{1\rho}$ values decreased as the temperature increased, and then increased again at 200 K. Below 300 K, only the $^{13}$C $T_{1\rho}$ value for C1 vs. the inverse temperature showed a minimum of 28.58 ms at 200 K, which implies the existence of active molecular motions at low temperatures. $\tau_C$ values on a logarithmic scale, as obtained by Eq. (2) vs. 1000/T, were plotted (inset of Fig. 7). The $E_a$, depending on the molecular dynamics of $^{13}$C, was measured to be 8.59 ± 0.47 kJ/mol. The $^{13}$C $E_a$ value was approximately twice that of $^1$H $E_a$.

## Discussion

$^1$H and $^{13}$C NMR $T_{1\rho}$ values in $[NH_3(CH_2)_3NH_3]Me Br_4$ (*Me*=Cu, Zn, and Cd) crystals were compared and discussed with previously reported results[27,35]. In single crystals of $[NH_3(CH_2)_3NH_3]Me Br_4$ (*Me*=Cu, Zn, and Cd), the crystal structure, phase transition temperature, and $T_{1\rho}$ for $^1$H and $^{13}$C when the cation lengths are the same and the *Me* is different, are shown in Table 1. The changes in the chemical shifts of both $^1$H and $^{13}$C for three crystals with temperature are shown in Supplementary Information 2 and 3. When Zn and Cd were included, the $^1$H and $^{13}$C chemical shifts were similar, whereas when Cu was included, the chemical shifts were different. The differences in the chemical shifts are due to the differences in the electron structures of the metal ions, *Me*. $Cu^{2+}$ has one electron, outside the closed *d*-shell. $Zn^{2+}$ and $Cd^{2+}$ have two electrons outside its closed shell[37].

$^1$H $T_{1\rho}$ values with a paramagnetic $Cu^{2+}$ ion have a very different trend from those of $Zn^{2+}$ and $Cd^{2+}$ without the paramagnetic ion; Zn and Cd show a very similar trend and indicate temperature dependence alone (see Fig. 8). $T_{1\rho}$ has a very less value because of the $Cu^{2+}$-containing paramagnetic ions. Because $T_{1\rho}$ is inversely proportional to the square of the magnetic moment of the paramagnetic $Cu^{2+}$ ions, the value is in the order of a few milliseconds. Unlike the $^1$H $T_{1\rho}$ values, the $^{13}$C $T_{1\rho}$ values when Zn is included are in the order of 10 ms, and the $^{13}$C $T_{1\rho}$ values when Cu and Cd are included have a very long order of 100 ms, and are sensitive to temperature, as shown in Fig. 9. From these results, the effect of paramagnetic ions was directly affected by $^1$H, which is close to that of Cu, but $^{13}$C $T_{1\rho}$ was not significantly affected by the paramagnetic ions. In addition, the structures of Cu and Cd are related to the octahedral $Me Br_6$, and the structure of Zn is related to tetrahedral $Me Br_4$. The $^{13}$C
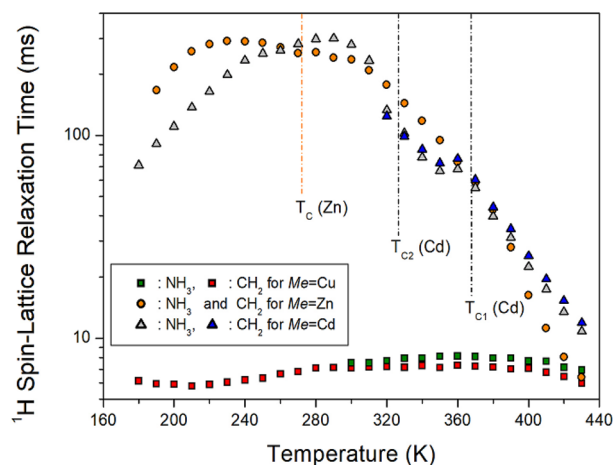
**Figure 8.** $^1$H NMR spin–lattice relaxation times $T_{1\rho}$ of $[NH_3(CH_2)_3NH_3]Me Br_4$ ($Me$ = Cu, Zn, and Cd) as a function of temperature.
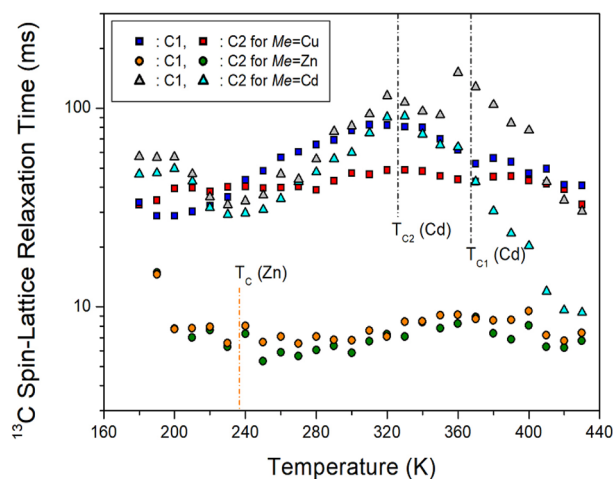


**Figure 9.** $^{13}$C NMR spin–lattice relaxation times $T_{1\rho}$ of $[NH_3(CH_2)_3NH_3]Me Br_4$ ($Me$ = Cu, Zn, and Cd) as a function of temperature.

$T_{1\rho}$ values in $[NH_3(CH_2)_3NH_3]CuBr_4$ and $[NH_3(CH_2)_3NH_3]CdBr_4$ with the two-dimensional octahedral $Me Br_6$ structure have longer values than those in $[NH_3(CH_2)_3NH_3]ZnBr_4$ with the zero-dimensional structure of the tetrahedral $Me Br_4$. The $^1$H $T_{1\rho}$ is affected by the paramagnetic ion of the cation, and the $^{13}$C $T_{1\rho}$ is thought to be affected by the $MeX_4$ or $MeX_6$ structure of the anion.

## Conclusion

To investigate the structural, thermal, and physical properties of the lead-free hybrid perovskite $[NH_3(CH_2)_3NH_3]$ $CuBr_4$ crystal, we performed XRD, DSC, TGA, optical polarizing microscopy, and NMR spectroscopy. First, the monoclinic structure of this crystal was confirmed by XRD, and its thermodynamic stability was observed at approximately 500 K without phase transition. Second, the NMR chemical shifts were due to the local field around the resonating nucleus in the crystals, and the chemical shifts in the $^1$H and $^{13}$C NMR spectra indicated changes in the crystallographic geometry. The $^1$H chemical shifts of $NH_3$ changed significantly with temperature compared to those of the $CH_2$ because the structural environment around the $^1$H of $NH_3$ changed to a greater degree than the structural environment around the $^1$H of $CH_2$. In addition, the $^{13}$C chemical shifts for C1 increased slowly with increasing temperature, whereas the chemical shifts for C2 shifted significantly compared to C1. Consequently, the large changes in the $^1$H chemical shifts of $NH_3$ and the chemical shift of C2 close to N were affected by the N−H···Br hydrogen bonds owing to the extensive changes in the structural geometry of $CuBr_4$. Finally, $^1$H and $^{13}$C $T_{1\rho}$ showed very similar trends for temperature changes; however, the $^1$H $T_{1\rho}$ values were approximately 10 times shorter than the $^{13}$C $T_{1\rho}$ values. $T_{1\rho}$ values show that the energy transfer, with a large thermal displacement around the $^1$H atoms of the cation, is very short. $E_a$ values for $^1$H and $^{13}$C at low temperatures were 4.25 and 8.59 kJ/mol, respectively, indicating that the value for $^1$H was smaller.

The detailed elucidation of these physical properties is expected to greatly facilitate the development of potential eco-friendly material applications. In the future, we plan to study [NH$_3$(CH$_2$)$_3$NH$_3$]$Me$I$_4$, which may be more suitable candidate for solar cells. Furthermore, as the most popular approaches to materials design, we plan to expand and study a high-quality film and relevant characterizations.

## Data availability

The datasets generated and/or analysed during the current study are available from the corresponding author on reasonable request.

## References

1. Hermes, I. M. *et al.* Ferroelastic fingerprints in methylammonium lead iodide perovskite. *J. Phys. Chem. C* **120**, 5724 (2016).
2. Abdel-Aal, S. K., Abdel-Rahman, A. S., Kocher-Oberlehner, G. G., Ionov, A. & Mozhchil, R. Structure, optical studies of two-dimensional hybrid perovskite for photovoltaic applications. *Acta Cryst. A* **70**, C1116 (2017).
3. Strelcov, E. *et al.* CH$_3$NH$_3$PbI$_3$ perovskites: ferroelasticity revealed. *Sci. Adv.* **3**, e1602165 (2017).
4. Liu, Y. *et al.* Chemical nature of ferroelastic twin domains in CH$_3$NH$_3$PbI$_3$ perovskite. *Nat. Mater.* **17**, 1013 (2018).
5. Lee, J., Lee, W., Kang, K., Lee, T. & Lee, S. K. Layer-by layer structural identification of 2D ruddlesden-popper hybrid lead iodide perovskites by solid-state NMR spectroscopy. *Chem. Mater.* **33**, 370 (2021).
6. Su, C. *et al.* Hybrid optical-electrical perovskite can be a ferroelastic semiconductor. *CCS Chem.* **3**, 2021 (2021).
7. Xie, Y. *et al.* The soft molecular polycrystalline ferroelectric realized by the fluorination effect. *J. Am. Chem. Soc.* **142**, 12486 (2020).
8. Fu, D.-W. *et al.* High-TC enantiometric ferroelectric based on homochiral dabco-derivatives (Dabco=1,4-Diazabicyclo[2.2.2.] octane. *Angew. Chem. Int. Ed.* **59**, 17477 (2020).
9. Gonzalez-Carrero, S., Galian, R. E. & Perez-Prieto, J. Organometal halide perovskites: bulk low-dimension materials and nano-particles. *Part. Syst. Charact.* **32**, 709 (2015).
10. Abdel-Adal, S. K., Kocher-Oberlehner, G., Ionovand, A. & Mozhchil, R. N. Effect of organic chain length on structure, electronic composition, lattice potential energy, and optical properties of 2D hybrid perovskites [(NH$_3$)(CH$_2$) $_n$ (NH$_3$)]CuCl$_4$, *n* = 2–9. *Appl. Phys. A* **123**, 531 (2017).
11. Liu, W. *et al.* Giant two-photon absorption and its saturation in 2D organic-inorganic perovskite. *Adv. Opt. Mater.* **5**, 1601045 (2017).
12. Staskiewicz, B. & Staskiewicz, A. The influence of the relative thermal expansion and electric permittivity on phase transitions in the perovskite-type bidimensional layered NH$_3$(CH$_2$)$_3$NH$_3$CdBr$_4$ compound. *J. Phys. Chem. Solids* **106**, 65 (2017).
13. Czupinski, O., Ingram, A., Kostrzewa, M., Przeslawski, J. & Czapla, Z. On the structural phase transition in a perovskite-type dia minopropanetetrachlorocuprate(II) NH$_3$(CH$_2$)$_3$NH$_3$CuCl$_4$ crystal. *Acta Phys. Pol., A* **131**, 304 (2017).
14. Elseman, M. *et al.* Copper-substituted lead perovskite materials constructed with different halides for working (CH$_3$NH$_3$)$_2$CuX$_4$-based perovskite solar cells from experimental and theoretical view. *ACS Appl. Mater. Interfaces* **10**, 11699 (2018).
15. Aramburu, J. A., Garcia-Fernandez, P., Mathiesen, N. R., Garcia-Lastra, J. M. & Moreno, M. Changing the usual interpretation of the structure and ground state of Cu$^{2+}$ layered perovskites. *J. Phys. Chem. C* **122**, 5071 (2018).
16. Przeslawski, J., Czapla, Z., Crofton, M. & Dacko, S. On the "inverted" phase transitions in ferroic crystals containing propylenedi-ammonium cations. *Ferroelectrics* **534**, 220 (2018).
17. Wang, Y. *et al.* (1,4-Butyldiammonium)CdBr$_4$: a layered organic–inorganic hybrid perovskite with a visible-blind ultraviolet photoelectric response. *Inorg Chem Front* **5**, 2450 (2018).
18. Liang, D., Lian, X., Li, X. & Luo, B. Pb alloying enables efficient broadband emission of two dimensional [NH$_3$(CH$_2$)$_4$NH$_3$]CdBr$_4$. *J. Solid State Chem.* **293**, 121772 (2021).
19. Mitzi, D. B. Templating and structural engineering in organic-inorganic perovskites. *J. Chem. Soc. Dalton Trans* **1**, 1 (2001).
20. Saikumar, S., Ahmad, J. J., Baumberg, G. & Vijaya Prakash, G. Fabrication of excitonic luminescent inorganic-organic hybrid nano- and microcrystals. *Scr. Mater.* **67**, 834 (2012).
21. Ahmad, S., Hanmandlu, C., Kanaujia, P. K. & Vijaya Prakash, G. Direct deposition strategy for highly ordered inorganic organic perovskite thin films and their optoelectronic applications. *Opt. Mater. Express* **4**, 1313 (2014).
22. Wei, Y., Audebert, P., Galmiche, L., Lauret, J. S. & Deleporte, E. Photostability of 2D organic–inorganic hybrid perovskites. *Materials* **7**, 4789 (2014).
23. Chen, Q. *et al.* Under the spotlight: the organic–inorganic hybrid halide perovskite for optoelectronic applications. *Nano Today* **10**, 355 (2015).
24. Svane, K. L. *et al.* How strong is the hydrogen bond in hybrid perovskites?. *J. Phys. Chem. Lett.* **8**, 6154 (2017).
25. Lim, A. R. & Kim, S. H. Physicochemical property investigations of perovskite-type layer crystals [NH$_3$(CH$_2$)$_n$NH$_3$]CdCl$_4$ (*n* = 2, 3, and 4) as a function of length *n* of CH$_2$. *ACS Omega* **6**, 27568 (2021).
26. Zang, W. & Xiong, R.-G. Ferroelectric metal–organic frameworks. *Chem. Rev.* **112**, 1163 (2012).
27. Lim, A. R., Kim, S. H. & Joo, Y. L. Physicochemical properties and structural dynamics of organic–inorganic hybrid [NH$_3$(CH$_2$)$_3$NH$_3$]ZnX$_4$ (X = Cl and Br) crystals. *Sci. Rep.* **11**, 8408 (2021).
28. Halvorson, K. & Willett, R. D. Structures of ethylenediammonium tetrabromocuprate (II) and propylenediammonium tetrabro-mocuprate (II). *Acta Cryst. C* **44**, 2071 (1988).
29. Snively, L. O., Haines, D. N., Emerson, K. & Drumheller, J. E. Two-halide superexchange in [NH$_3$(CH$_2$)$_n$NH$_3$]CuBr$_4$ for n=3 and 4. *Phys. Rev. B* **26**, 5245 (1982).
30. Straatman, P., Block, R. & Jansen, L. Theoretical analysis of double-halide superexchange in layered solids of the compounds [NH$_3$(CH$_2$)$_n$NH$_3$]CuBr$_4$ with n=3 and 4. *Phys. Rev. B* **29**, 1415 (1984).
31. Kite, T. & Drumheller, J. E. Electron paramagnetic resonance of the eclipsed layered compounds NH$_3$(CH$_2$)$_n$NH$_3$CuBr$_4$ with n = 2, 3, 4. *J. Mag. Reson.* **54**, 253 (1983).
32. Kallel, A., Fail, J., Fuess, H. & Daoud, A. 1,3-propanediammonium tetrachlorozincate (II). *Acta Cryst. B* **36**, 2788 (1980).
33. Ishihara, H. *et al.* Isolated versus condensed anion structure II; the influence of the cations (1,3-propanediammonium, 1,4-phe-nylendiammonium, and n-propylammonium) on structures and phase transitions of CdBr 2–4 salts A 79,81Br NQR and X-ray structure analysis. *Z. Naturforsch. A: Phys. Sci.* **51**, 1216 (1996).
34. Ishihara, H. *et al.* NQR, NMR, and DSC study of [NH3(CH2)3NH3]CdBr 4. *Chem. Lett.* **25**, 371–372 (1996).
35. Lim, A. R. Thermal, ferroelastic, and structural properties near phase transitions of organic–inorganic perovskite type [NH$_3$(CH$_2$)$_3$NH$_3$]CdBr$_4$ crystals. *RSC Adv.* **11**, 17622 (2021).
36. Abragam, A. *The Principles of Nuclear Magnetism* (Oxford University Press, 1961).
37. Koenig, J. L. *Spectroscopy of Polymers* (Elsevier, 1999).
38. Harris, R. K. *Nuclear Magnetic Resonance Spectroscopy* (Pitman Pub., London, 1983).

39. Bloembergen, N., Purcell, E. M. & Pound, R. V. Relaxation effects in nuclear magnetic resonance absorption. *Phys. Rev.* **73**, 679 (1948).

## Acknowledgements

## Author contributions

A.R.L. designed the project and performed. N.M.R. experiments. L.K.K. performed. D.S.C. and T.G.A. experiments.

## Competing interests

The authors declare no competing interests.

## Additional information

**Supplementary Information** The online version contains supplementary material available at https://doi.org/10.1038/s41598-022-12832-y.

**Correspondence** and requests for materials should be addressed to A.R.L.

**Reprints and permissions information** is available at www.nature.com/reprints.

**Publisher's note** Springer Nature remains neutral with regard to jurisdictional claims in published maps and institutional affiliations.